Flexural Strengthening of RC Beams using Hybrid Composite Plate (HCP): Experimental and Analytical Study

Esmaeel Esmaeeli, Joaquim A. O. Barros

ISISE, Dept. Civil Eng., University of Minho, Guimarães, Portugal

Contacts of corresponding author:

Esmaeel Esmaeeli

ISISE, Dep. Civil Eng., School Eng., University of Minho

Campus de Azurém,

4800-058 Guimarães, Portugal

Tel: +351 917 40 90 75

Email: esmaeeli_civil@outlook.com

Abstract:

Hybrid Composite Plate (HCP) is a reliable recently proposed retrofitting solution for concrete structures, which is composed of a strain hardening cementitious composite (SHCC) plate reinforced with Carbon Fibre Reinforced Polymer (CFRP). This system benefits from the synergetic advantages of these two composites, namely the high ductility of SHCC and the high tensile strength of CFRPs. In the material-structural of HCP, the ultra-ductile SHCC plate acts as a suitable medium for stress transfer between CFRP laminates (bonded into the pre-sawn grooves executed on the SHCC plate) and the concrete substrate by means of a connection system made by either chemical anchors, adhesive, or a combination thereof. In comparison with traditional applications of FRP systems, HCP is a retrofitting solution that (i) is less susceptible to the detrimental effect of the lack of strength and soundness of the concrete cover in the strengthening effectiveness; (ii) assures higher durability for the strengthened elements and higher protection to the FRP component in terms of high temperatures and vandalism; and (iii) delays, or even, prevents detachment of concrete substrate. This paper describes the experimental program carried out, and presents and discusses the relevant results obtained on the assessment of the performance of HCP strengthened reinforced concrete (RC) beams subjected to flexural loading. Moreover, an analytical approach to estimate the ultimate flexural capacity of these beams is presented, which was complemented

with a numerical strategy for predicting their load-deflection behaviour. By attaching HCP to the beams' soffit, a significant increase in the flexural capacity at service, at yield initiation of the tension steel bars and at failure of the beams can be achieved, while satisfactory deflection ductility is assured and a high tensile capacity of the CFRP laminates is mobilized. Both analytical and numerical approaches have predicted with satisfactory agreement, the load-deflection response of the reference beam and the strengthened ones tested experimentally.

Keywords: A. Carbon fibre; A. Laminates; C. Numerical analysis; D. Mechanical testing; Strain-hardening cementitious composite (SHCC).

1. Introduction

Nowadays, reports on extensive studies of the applications of fibre Reinforced Polymers (FRPs) in both laboratory and practical scales can be found [1-3]. This widespread application of FRP for structural strengthening is mainly due to its practical feasibility and high strength to weight ratio. The long-term durability, thermal stability, and vulnerability against vandalism are, however, concerns that need to be properly addressed for a still more extensive use of the FRP [4-6]. Premature debonding of FRP systems at the interface with substrate, or detachment with concrete cover attached (rip-off), are other causes that limits the maximum tensile strain that FRP systems can sustain. In an effort to delay or overcome this problem, various configurations of mechanical anchors can be found in literature [7, 8], but they may promote the risk of premature rupture of FRP material, since a stress concentration at the anchored zone of the FRP system is expectable.

In the last few years, a new retrofitting system nominated as Hybrid Composite Plate (HCP) was developed to overcome, even partially, the above-mentioned shortcomings of FRPs [9]. This hybrid system is composed of a strain hardening cementitious composite (SHCC) plate reinforced either by externally bonded CFRP sheets, $HCP^{(s)}$, or near surface mounted CFRP laminates, $HCP^{(L)}$. SHCC is capable of developing higher tensile strengths by further stretching beyond the onset of the first crack, which offers a high tensile strain hardening capacity. Thus, as depicted schematically in Figure 1, HCP integrates the synergetic advantages of these two composites, namely strength and ductility, in retrofitting of reinforced concrete (RC) structures [10]. Thanks to the high ductility of SHCC, this prefabricated plate (with a thickness ranging from 15 to 25 mm) can be attached to the substrate by means of anchors, adhesives or a combination thereof to transfer forces between HCP and RC substrate. HCPs were developed to suppress, even if partially, the above-mentioned shortcomings of bonded FRP systems in structural strengthening. For example, in the case of $HCP^{(L)}$, SHCC provides a minimum cover of 8 mm to the laminates, which provides insulation for both FRP and bonding material used in the structure of an HCP, so the system can endure higher levels of temperature in comparison to traditional applications of FRP systems. Up to the rupture strain of CFRP materials, which is often below 2%, impermeable fine diffused cracks are formed in the SHCC, with a maximum crack width limited to 0.1 mm, which potentially assures a long-time performance for the constituents of the HCP system, and enhances the durability of the elements to be strengthened (see Figure 1). Results of experimental tests on HCP retrofitted RC elements indicated a

promising performance of this system, since a substantial increase was attained in terms of flexural and shear capacity of RC beams, and energy dissipation and lateral load carrying capacities of RC beam-column joints under seismic loading [9, 11-13].

This paper describes an experimental program and presents and discusses the relevant obtained results on the assessment of the effectiveness of $HCP^{(L)}$ for the flexural strengthening of under-reinforced RC beams. Moreover, an analytical formulation to predict the ultimate moment capacity of such strengthened beams is presented. Finally, by employing a section-layer analysis technique, the moment-curvature of each of the retrofitted beams was obtained, and then was introduced into a numerical model to estimate the load-deflection response of these RC beams. To evaluate the accuracy of the adopted numerical approach, the estimated results were then compared to the results of the experimental tests.

2. Experimental Program

To experimentally assess the efficacy of $HCP^{(L)}$, for the flexural strengthening of the RC beams, seven under-reinforced RC beams with identical geometry and flexural and shear steel reinforcing ratios, as shown in Figure 2, was cast using a batch of concrete. One of the beams was considered as the reference specimen (FB_R), and its flexural behaviour was characterized by performing a four-point bending test in as-built condition. The other six beams were strengthened by attaching either a SHCC plate or a $HCP^{(L)}$ to their tension face (the face of the beams subjected to tension under bending deformation). Except for FB0_G, which was the only beam strengthened by an adhesively bonded SHCC plate, the rest of the beams were strengthened by using $HCP^{(L)}$. Details of the adopted strengthening strategies are shown in Figure 3 and summarized in Table 1. The $HCP^{(L)}$ of all of these beams had identical length and thickness as the SHCC plate of FB0_G, however, these strengthened beams were categorized in two main groups. The $HCP^{(L)}$ used to strengthen the beams of the first group had only two CFRP laminates, while the specimens of the second group were strengthened using $HCP^{(L)}$s containing four CFRP laminates. The first group of strengthened beams was composed of three specimens (FB2_B, FB2_G and FB2_BG), whose differences are limited to the technique adopted to attach the $HCP^{(L)}$ to their soffit. In the two beams forming the second group (FB4_BG_Phi8 and FB4_BG_Phi10), a combination of chemical anchors and epoxy adhesive was used to attach the $HCP^{(L)}$. However, the attaching systems adopted for the beams in the second group were different considering the size and the configuration of the anchors. The arrangement of CFRP laminates in

the structure of $HCP^{(L)}$ was another difference for the beams of this group. In the case of FB4_BG_Phi10, a double-CFRP laminate was bonded into each of the two pre-sawn grooves on the $HCP^{(L)}$, while the $HCP^{(L)}$ used for the beam FB4_BG_Phi8 had a double-CFRP laminate at the central groove, and two single-CFRP laminates at the two lateral grooves. For this latter beam a staggered configuration of the chemical anchors was adopted. Details of pre-sawn grooves containing a double or a single configuration of CFRP laminate are shown in Figure 4.

2.1. Strengthening Strategy

To enhance the bond quality at the interface of the epoxy adhesive and the beam's concrete substrate, the tension face of the beams was sand-blasted to remove 1 to 2 mm of cement paste and to partially expose the aggregates. The beams were positioned upside-down to facilitate attaching the strengthening plates to their tension face in laboratory conditions. Therefore, at this position, the strengthening plates were attached to the top face of the beams. When chemical anchors were used, their positions were marked in the $HCP^{(L)}$, and then holes were executed by drilling process. Afterwards, each perforated $HCP^{(L)}$ was placed on its corresponding beam and the positions of the holes were mapped on the beams' top face. Prior to placing the anchors, the holes were injected with a fast curing chemical adhesive to approximately fill two-thirds of their depth. Before placing the $HCP^{(L)}$ on the beam, the epoxy adhesive was spread on the contact surfaces of both $HCP^{(L)}$ and beam's concrete substrate. It should be noted that the contact face of the $HCP^{(L)}$ was the one in which CFRP laminates were installed. After placing the $HCP^{(L)}$ on the tension face of the beam, by fastening the nuts the epoxy adhesive was forced to flow and fill uniformly the entire contact surfaces of the $HCP^{(L)}$ and the beam. For the beams in which epoxy adhesive was the only component used for attaching the strengthening scheme, the plate was pressed against the beam in order to force adhesive to flow between the contact faces. Finally, some weights were put on top of the plate aiming to hold it in its position. For in-situ application, a few number of anchors is recommended to facilitate the installation process of the strengthening plate. To assure that the bonding epoxy adhesive attained its maximum mechanical properties, a curing period of adhesive at least seven days was considered before testing the corresponding beam. Prior to testing the beams, a torque of 30 and 20 N·m was applied to pos-tension the anchor rods of 10 and 8 mm, respectively.

2.2. Test Setup and Monitoring Instruments

A four-point bending test setup, schematically represented in Figure 5, with a constant displacement rate of 0.01 mm/sec controlled by the internal Linear Voltage Differential Transformer (LVDT) of the jack, was adopted to experimentally evaluate the flexural response of the beams. The deflections at the mid-span and at the loaded sections of the tested beams were measured using three LVDTs supported on a Japanese yoke (a steel bar fixed to the mid-height of the beam at the sections coinciding with the beam's supports, using a pin connection at one end and a rolling connection at the other end). Strain gauges were used to measure the local deformation for a limited number of locations along the longitudinal reinforcement. For all specimens, including reference beam, a strain gauge (SM) was bonded to the mid-length of one of the longitudinal tension steel bars. For the specimens strengthened with $HCP^{(L)}$, strain gauges were used to measure the tensile strain in CFRP laminates at mid-span (PM), under the loaded section at the right span of the beam (PL), and at the theoretical curtailment section (PTC). Only a few numbers of strain gauges was used to minimize the disturbance of the bond between CFRP laminates and surrounding SHCC along the strengthened length of the beam. However, some of these strain gauges did not function properly, possibly due to the damages introduced by fastening the anchors.

2.3. Material Properties

The self-compacting SHCC was composed of a cementitious mortar reinforced with 2% in volume of short discrete PVA fibres. The fibres used in this study (supplied by Kuraray Company with designation RECs 15×8) had a length and a diameter of 8 and 0.04 mm, respectively. The average tensile stress at crack initiation and at ultimate tensile strength of the SHCC was 2.75 and 3.5 MPa, respectively, with a tensile strain capacity of 1.54%. Details on mixture ingredients, mixing process and mechanical characterization of the SHCC can be found in [14, 15]. From uniaxial tensile tests carried out according to the recommendations of ISO 527-2:2012 [16] on six dumbbell-shaped S&P 220 epoxy resin cured for seven days, an average tensile strength of 18 MPa and average modulus of elasticity of 6.8 GPa were obtained. Tensile properties of CFRP laminate (S&P laminate CFK 150/2000) with a cross section of 1.4×10 mm^2 were characterized following the procedures proposed in ISO 527-5:2009 [17]. From the tests executed in six coupons, average values of 2689 MPa, 1.6% and 164.7 GPa were obtained for the tensile strength, strain at CFRP rupture and modulus of elasticity, respectively. In order to obtain the modulus of elasticity and the

compressive strength of the concrete used for casting the beams, four cylinders of 150 mm in diameter and 300 mm in depth at the age of 90 days were tested following the specification of LNEC E397-1993 [18] and EN 12390-3 2009 [19], respectively. According to the results of these tests, an average modulus of elasticity of 32.52 GPa and an average compressive strength of 31.26 MPa were obtained. Properties of the longitudinal steel bars were determined by means of tensile tests according to ISO 15630-1-2010 [20]. From the results of the tensile tests on four specimens of 10 mm diameter steel bars, average values of 536 MPa, 629 MPa and 215.8 GPa were determined as the yield stress, ultimate strength, and modulus of elasticity, respectively. For the HCP$^{(L)}$ applied with anchors, a Hilti® system was utilized, composed of a fast curing resin HIT-HY 200A and steel anchor rods. Two types of anchor rods were used, 8 and 10 mm in diameter with specifications of HIT-V-5.8 M8X110 and HIT-V-8.8 M10X190, respectively. According to the classification of the steel grades of the ASTM, a notation of 5.8 indicates steel with average tensile yield stress of 400 MPa and an average ultimate tensile strength of 500 MPa. The notation of 8.8 then refers to the steel with average tensile yield stress of 640 MPa and average tensile ultimate strength of 800 MPa.

2.4. Design Procedure of the Retrofitting Systems

Figure 6 shows the schematic stress-strain distribution along the depth of the cross-section of an HCP$^{(L)}$ strengthened beam (see the list of notations of this paper for the physical meaning of each symbol used in this figure and herein after). Based on the assumption that plane sections remain plane after bending, and assuming a perfect bond between constituent materials, a linear distribution of strain along the depth of the cross-section is adopted (see Figure 6b). The number of CFRP laminates utilized in HCP$^{(L)}$ for the strengthening of the first and second group of beams was determined taking into account the required section area to attain a balance failure of the strengthened beam. The balance failure mode is defined as a simultaneous CFRP rupture $\left(\varepsilon_f = \varepsilon_f^r\right)$ and crushing of concrete in compressive block $(\varepsilon_{cc}^t = \varepsilon_{cc}^u)$. It can be assumed that for this mode of failure, tension steel bars are already yielded $\left(\varepsilon_{st} \geq \varepsilon_{st}^y\right)$. By employing the equivalent rectangular compressive stress distribution recommended by EC2 [21] and considering the force components indicated in Figure 6b and Figure 6c, the state of equilibrium of the section $(\sum F = 0)$ can be formulated based on strain compatibility and stress distribution along the depth of the section, resulting equations (1) to (7). The position of the neutral axis, n, can be also calculated by using equation (8). After replacing n in the equation (7) and solving it, the balance section area of CFRP laminates, A_f^b, can be

obtained from equation (9). Note that in this approach the average concrete compressive strength, f_{cc}^{m}, is used in place of its design value, f_{cd}. For a concrete with a characteristic strength equal to or lower than 50 MPa, according to the section 3 of EC2 [21] values of 0.8, 1.0 and -0.0035 are adopted for λ, η and ε_{cc}^{u}, respectively. To simplify, the analysis, the contribution of the part of concrete in tension is neglected in static equilibrium of the section. Moreover, tensile behaviour of the SHCC and the steel bars are assumed to be elastic-perfectly plastic with maximum strength equal to the stress at the first cracking of the SHCC, f_{sh}^{cr}, and the yielding of tension steel bars, f_{st}^{y} (the behaviour of steel under uniaxial compression was considered identical to its tensile response). According to this strategy, $A_f^b = 64.4$ mm^2 was obtained, and four CFRP laminates providing $A_f = 56$ mm^2 were adopted for the HCP$^{(L)}$ of the beams in the second group and half of this reinforcement, $A_f = 28$ mm^2, was assigned to the HCP$^{(L)}$ of the beams in the first group.

$$\varepsilon_{sc} = \varepsilon_{cc}^{u}\frac{(n-d')}{n} \tag{1}$$

$$F_{cc} = \lambda n b f_{cc}^{m} \quad \text{with} \quad \lambda = 0.8 \qquad \text{EC2 [21]} \tag{2}$$

$$F_{sc} = \begin{cases} E_{sc}A_{sc}\varepsilon_{cc}^{u}\dfrac{(n-d')}{n} & \varepsilon_{sc} \leq \varepsilon_{sc}^{y} \\ f_{sc}^{y}A_{sc} & \varepsilon_{sc} > \varepsilon_{sc}^{y} \end{cases} \tag{3}$$

$$F_{st} = A_{st}f_{st}^{y} \tag{4}$$

$$F_f = A_f^b f_f^r \tag{5}$$

$$F_{sh} = A_{sh}f_{sh}^{cr} \tag{6}$$

$$F_{cc} + F_{sc} + F_f + F_{st} + F_{sh} = 0 \tag{7}$$

$$n = \frac{\varepsilon_{cc}^{u}d_f}{(\varepsilon_{cc}^{u} - \varepsilon_{f}^{r})} \tag{8}$$

$$A_f^b = \begin{cases} -\left(0.8nbf_{cc}^{m} + E_{sc}A_{sc}\varepsilon_{cc}^{u}\frac{(n-d')}{n} + A_{st}f_{st}^{y} + A_{sh}f_{sh}^{cr}\right)/\left(E_f\varepsilon_f^r\right), & \varepsilon_{sc} \leq \varepsilon_{sc}^{y} \\ -\left(0.8nbf_{cc}^{m} + f_{sc}^{y}A_{sc} + A_{st}f_{st}^{y} + A_{sh}f_{sh}^{cr}\right)/\left(E_f\varepsilon_f^r\right), & \varepsilon_{sc} > \varepsilon_{sc}^{y} \end{cases} \tag{9}$$

2.4.1. Flexural Capacity of the HCP$^{(L)}$ Strengthened Beams

Since for both groups of strengthened beams, the total section areas of CFRP laminates utilized in the structure of the HCP$^{(L)}$ were less than A_f^b, the rupture of the CFRP laminates is the expected failure mode, provided that detachment of the HCP$^{(L)}$ is not the prevailing failure. Considering that at the failure of these

beams, the maximum concrete compressive strain is lower than ε_{cc}^{u}, the moment capacity (M_R) is calculated adopting two different stress distribution for concrete in compression: (i) constant stress distribution (Whitney block), and (ii) nonlinear stress distribution. Further, the flexural capacities obtained from these approaches are compared in order to verify the accuracy of prediction based on using an equivalent compression block as a simplified method. In both of these strategies, the flexural capacity at CFRP rupture is calculated assuming that tension steel bars are already yielded and the compression steel bars are still in their linear-elastic regime. The assumptions used for the tensile contribution of the concrete, the idealized stress-strain relationships for SHCC and steel bars in the calculation of balance amount of CFRP laminates are applied herein as well.

Rectangular compressive stress distribution: considering Figure 6a to Figure 6c and simplifying the equations of static equilibrium of the section ($\sum F = 0$), developed based on strain compatibility and stress distribution as indicated in equations (10) to (20), the depth of neutral axis, n, can be found by solving the quadratic equation (21). Constants of this latter equation are introduced in equations (22) to (24). Thus, the depth of neutral axis, n, can be calculated from equation (25). Finally, the flexural capacity (M_R) of the beams of groups I and II can be calculated from equation (26).

$$\varepsilon_f = \varepsilon_f^r \tag{10}$$

$$\varepsilon_{cc} = \varepsilon_f^r \frac{n}{(n - d_f)} \tag{11}$$

$$\varepsilon_{sc} = \varepsilon_f^r \frac{(d' - n)}{(d_f - n)} \tag{12}$$

$$\varepsilon_{sc} = \varepsilon_f^r \frac{(d' - n)}{(d_f - n)} \tag{13}$$

$$F_{cc} = \lambda n b f_{cc}^m \quad \text{with} \quad \lambda = 0.8 \qquad \text{EC2 [21]} \tag{14}$$

$$F_{sc} = E_{sc} A_{sc} \left[\varepsilon_f^r \frac{(d' - n)}{(d_f - n)} \right] \qquad \varepsilon_{sc} < \varepsilon_{sc}^y \tag{15}$$

$$F_{st} = A_{st} f_{st}^y \qquad \varepsilon_{st} \geq \varepsilon_{st}^y \tag{16}$$

$$F_f = A_f f_f^r \tag{17}$$

$$F_{sh} = A_{sh} f_{sh}^{cr} \tag{18}$$

$$F_{cc} + F_{sc} + F_f + F_{st} + F_{sh} = 0 \tag{19}$$

$$-\lambda b f_{cc}^{m} n^2 - \left(A_{st} f_{st}^{y} + A_f f_f^r + A_{sh} f_{sh}^{u} + E_{sc} A_{sc} \varepsilon_f^r - \lambda b f_{cc}^{m} d_f\right) n + \left(A_{st} f_{st}^{y} + A_f f_f^r + A_{sh} f_{sh}^{cr}\right) d_f + E_{sc} A_{sc} \varepsilon_f^r d' = 0 \tag{20}$$

$$\boldsymbol{A} n^2 + \boldsymbol{B} n + \boldsymbol{C} = 0 \tag{21}$$

$$\boldsymbol{A} = -\lambda b f_{cc}^{m} \tag{22}$$

$$\boldsymbol{B} = -\left(A_{st} f_{st}^{y} + A_f f_f^r + A_{sh} f_{sh}^{cr} + E_{sc} A_{sc} \varepsilon_f^r - \lambda b f_{cc}^{m} d_f\right) \tag{23}$$

$$\boldsymbol{C} = \left(A_{st} f_{st}^{y} + A_f f_f^r + A_{sh} f_{sh}^{cr}\right) d_f + E_{sc} A_{sc} \varepsilon_f^r d' \tag{24}$$

$$n = \frac{-\boldsymbol{B} \pm \sqrt{\boldsymbol{B}^2 - 4\boldsymbol{A}\boldsymbol{C}}}{2\boldsymbol{A}} \tag{25}$$

$$M_R = A_{st} f_{st}^{y} d_{st} + A_f f_f^r d_f + A_{sh} f_{sh}^{cr} d_{sh} + E_{sc} A_{sc} \left[\varepsilon_f^r \frac{(d'-n)}{(d_f-n)}\right] d' + 0.5\lambda^2 n^2 b f_{cc}^{m} \tag{26}$$

Nonlinear compressive stress distribution: as it is presented schematically in Figure 6d and mathematically in equation (27), a parabolic stress distribution for concrete in compression block, recommended by EC2 [21], is also employed. By simplifying the equations of equilibrium of the section (see equations (28) to (37)), the depth of neutral axis, n, can be found by solving the cubic equation (38) with its constants presented in equations (39) to (44). The flexural capacity (M_R) of the beams of groups I and II can be calculated from equation (45). In this equation a is the distance of the location of the concrete compressive resultant force, F_{cc}, from neutral axis (see Figure 6d) and can be obtained from $\frac{\int_0^n x f_{cc} d_x}{\int_0^n f_{cc} d_x}$, as shown in equation (46).

$$f_{cc} = f_{cc}^{m}\left\{2\left(\frac{\varepsilon_{cc}}{\varepsilon_{cc}^{m}}\right) - \left(\frac{\varepsilon_{cc}}{\varepsilon_{cc}^{m}}\right)^2\right\} \qquad 0 \le \varepsilon_{cc} \le \varepsilon_{cc}^{u} \text{ (with } \varepsilon_{cc}^{m} \text{ being strain at } f_{cc}^{m}\text{)} \tag{27}$$

$$F_{cc} = b\int_0^n \left(f_{cc}^{m}\left\{2\left(\frac{\varepsilon_{cc}}{\varepsilon_{cc}^{m}}\right) - \left(\frac{\varepsilon_{cc}}{\varepsilon_{cc}^{m}}\right)^2\right\}\right) d_x \tag{28}$$

$$\varepsilon_{cc} = \varepsilon_f^r \frac{x}{(n - d_f)} \tag{29}$$

$$F_{cc} = -b\frac{f_{cc}^{m}}{(n-d_f)^2}\frac{\varepsilon_f^r}{\varepsilon_{cc}^{m}}\left[d_f n^2 - \left(1 - \frac{\varepsilon_f^r}{3\varepsilon_{cc}^{m}}\right) n^3\right] \tag{30}$$

$$F_{sc} = E_{sc} A_{sc}\left[\varepsilon_f^r \frac{(d'-n)}{(d_f-n)}\right] \qquad \varepsilon_{sc} < \varepsilon_{sc}^{y} \tag{31}$$

$$F_{st} = A_{st} f_{st}^{y} \qquad \varepsilon_{st} \ge \varepsilon_{st}^{y} \tag{32}$$

$$F_f = E_f A_f \varepsilon_f^r \tag{33}$$

$$F_{sh} = A_{sh} f_{sh}^{cr} \tag{34}$$

$$F_f + F_{st} + F_{sh} + F_{cc} + F_{sc} = 0 \tag{35}$$

$$T = F_f + F_{st} + F_{sh} \tag{36}$$

$$-b f_{cc}^{m} \frac{\varepsilon_f^r}{\varepsilon_{cc}^m}\left[d_f n^2 - \left(1 - \frac{\varepsilon_f^r}{3\varepsilon_{cc}^m}\right) n^3\right] - E_{sc} A_{sc} \varepsilon_f^r \left(n d_f - n^2 - d' d_f + d' n\right) + T {d_f}^2 + T n^2 - 2 T d_f n = 0 \tag{37}$$

$$\boldsymbol{A} n^3 + \boldsymbol{B} n^2 + \boldsymbol{C} n + \boldsymbol{D} = 0 \tag{38}$$

$$\gamma = b f_{cc}^{m} \frac{\varepsilon_f^r}{\varepsilon_{cc}^m} \tag{39}$$

$$\mu = E_{sc} A_{sc} \varepsilon_f^r \tag{40}$$

$$\boldsymbol{A} = \gamma \left(1 - \frac{\varepsilon_f^r}{3\varepsilon_{cc}^m}\right) \tag{41}$$

$$\boldsymbol{B} = \mu + T - \gamma d_f \tag{42}$$

$$\boldsymbol{C} = -\mu\left(d_f + d'\right) - 2 T d_f \tag{43}$$

$$\boldsymbol{D} = \mu d' d_f + T {d_f}^2 \tag{44}$$

therefore,

$$M_R = A_{st} f_{st}^{y} d_{st} + A_f f_f^r d_f + A_{sh} f_{sh}^{cr} d_{sh} + E_{sc} A_{sc} \left[\varepsilon_f^r \frac{(d' - n)}{(d_f - n)}\right] d' + \left[b \frac{f_{cc}^m}{(n - d_f)^2} \frac{\varepsilon_f^r}{\varepsilon_{cc}^m} \left(d_f n^2 - \left(1 - \frac{\varepsilon_f^r}{3\varepsilon_{cc}^m}\right) n^3\right)\right] (a - n) \tag{45}$$

$$a = \frac{n\left[\frac{2}{3} - \frac{n}{4(n - d_f)} \frac{\varepsilon_f^r}{\varepsilon_{cc}^m}\right]}{\left[1 - \frac{n}{3(n - d_f)} \frac{\varepsilon_f^r}{\varepsilon_{cc}^m}\right]} \tag{46}$$

The predicted M_R of the beams of groups I and II based on the abovementioned strategies are indicated and compared in Table 2. According to these results, the formulation based on equivalent compressive stress block (simplified method) estimates a flexural capacity similar to the one obtained using a nonlinear distribution of compressive stresses (a difference less than 0.5%).

3. Experimental Results and Discussions

The load-deflection curves registered for all the tested beams are presented in Figure 7. A summary including the values for the loads and their corresponding mid-span deflections at the onset of cracking (F_{cr} and δ_{cr}), at the yield of tension steel bars (F_y and δ_y), and at the failure of the beams (F_u and δ_u), is reported in Table 3. The service load, F_{400}, at deflection equal to the beam's span divided by 400 $\left(\delta_{400} = \frac{L_S}{400}\right)$, the deflection ductility ($\mu_\delta = \delta_{\mathrm{u}}/\delta_{\mathrm{y}}$), and the maximum strain measured by the strain gauge "PM" and the failure mode of each beam, are indicated in the same table. In the following sections, these results are used to discuss the failure mode and the overall behaviour of each beam, and also to compare the flexural behaviour of the strengthened beams.

3.1.1. Failure Modes and Overall Behaviour

The reference beam (FB_R) failed by crushing of compressive concrete at the mid-span following the yield of the tension steel bars. In the case of FB0_G, the maximum load, F_m, was reached at the onset of the yield of the tension steel bars. A sudden drop immediately after the yield of the steel bars in the load-deflection curve of FB0_G can be observed, followed by a gradual increase up to the yield load again, at a deflection of 16 mm. As the consequence of a further increase in the beam's deflection, the sequences of load drop and recovering continued, but with a decreasing trend in the recovered level of the maximum load. When the width of cracks in SHCC was wide enough for losing the strain hardening contribution, this process of stress redistribution along the beam stopped. At this stage, load was stabilized at an almost comparable level to the failure load of FB_R, and finally this beam failed by concrete crushing, at the left loaded section of the beam. Beam FB2_B failed with a splitting cracking in $HCP^{(L)}$, which progressed along the alignment of the chemical anchors. The onset of this failure mode was at the shear-out rupture of SHCC behind the closest anchor to the right support of the beam (see Figure 8a). Further, a splitting crack at the bearing zone of the second anchor initiated and progressed towards the first anchor. These sequences of splitting crack initiation and propagation between the adjacent anchors continued by increasing the beam's deflection, and with step-by-step load decay in the post-peak regime (see Figure 7). Specimen FB2_G failed by the detachment of $HCP^{(L)}$ with part of concrete cover bonded to it (Figure 8b). As demonstrated in this figure, the detachment of concrete cover originated from the location of a high stress concentration of a flexural-shear crack formed at the right shear-span of the beam close to the loaded section. This detachment

then progressed towards the end of the HCP$^{(L)}$, to the nearest beam's support. By further deflection of this beam, the detachment of the HCP$^{(L)}$ continued from its origin towards the beam's mid-span. This failure mode in an RC beam flexurally strengthened with a bonded plate/FRP to its tension face is often recognized as an intermediate flexural-shear crack induced detachment [22]. In the case of FB2_BG, the full tensile potential of the HCP$^{(L)}$ attached by means of epoxy adhesive and chemical anchors to the tension face of this beam was mobilized. Thus, at a location close to the loaded section at the right side of the beam, rupture of the CFRP laminates occurred. The full exploitation of HCP$^{(L)}$ was obtained despite of the onset of an IC detachment at the location of a flexural-shear crack (see Figure 9), which indicates a suitable contribution of chemical anchors in delaying the progress of this detachment.

Both beams in group II, FB4_BG_Phi10 and FB4_BG_Phi8, failed by the detachment of HCP$^{(L)}$ with part of concrete cover bonded to it. The progress of the detachment was similar to that observed in FB2_G, since an intermediate flexural-shear crack induced detachment was recognized for these beams as well, but at a load level much higher than the corresponding one registered in FB2_G. For both beams in this group the contribution of concrete cover for transferring the interfacial shear stresses developed between the strengthening layer and the tension face of the beam has decreased with the detachment progress. Consequently, a high tensile stress in the HCP$^{(L)}$ needed to be transferred to the beam's soffit by means of only shear resistance of chemical anchors. Due to the stress concentration at bearing zone of the last anchor, close to the termination of the HCP$^{(L)}$, a piece of SHCC behind the closest anchor to the right support of the beam was detached by a shear-out rupture. A high shear stress in the anchors caused their permanent deformation (observed by visual inspection at the failure), meaning that the anchors were already yielded. As a consequence of the yielding of the anchors, and therefore their excessive rotation, separation of HCP$^{(L)}$ was followed with a shear-punch mechanism at some of the anchored regions (see Figure 10). This secondary phenomenon, shear-punching, is expected to be delayed (or prevented) if washers with a larger clamping surface area are used.

3.1.2. Comparative behaviour

3.1.2.1. Load and Deflection at the First Crack

The load at the onset of the first crack, F_{cr}, was registered during testing of each beam and is reported in Table 3, together with its corresponding deflection, δ_{cr}. In comparison with the reference beam (FB_R),

an increase between 50% and 61% in F_{cr} for beams with a plate connected to their tension face by means of either epoxy adhesive or a combination of epoxy adhesive and chemical anchors (beams FB0_G, FB2_G, FB2_BG, FB4_BG_Phi10 and FB4_BG_Phi8) was obtained. The increase in corresponding deflection of these beams, δ_{cr}, was between 71% and 100% as registered for FB0_G and FB4_BG_Phi8, respectively. An increase of 42% in δ_{cr} of FB2_B for only 9% increase in the corresponding load, as compared to the results of the reference beam, was obtained. In fact, when HCP$^{(L)}$ is attached using only chemical anchors, in addition to stress concentration at the fastened locations, a substantial sliding between the strengthening plate and the beam is expected, resulting in a smaller contribution of the plate for the initial flexural stiffness of the beam when compared to the strengthening solutions where adhesive was used. The amount of this sliding depends on the roughness of the surfaces in contact, inter-laminar pressure caused by pos-tensioning of the anchors, distance between adjacent anchors, and also on the existing gaps between the anchors and the holes of the HCP$^{(L)}$.

3.1.2.2. Load and Deflection at the Yield of Tension Steel Bars

Since most of the strain gauges bonded to the tension steel bars did not functioned correctly, an apparent yield point was identified from the beams load-deflection curves. This apparent yield corresponded to the load at the onset of a substantial decrease in the slope of the post-cracking regime. According to this criterion, all of the strengthening techniques assured a higher yield load, F_y, compared to the corresponding value for FB_R. The maximum increase in F_y was 65%, registered in the beam FB4_BG_Phi8, and the minimum increase was 21%, which was attained by FB0_G. Both FB2_G and FB2_BG showed an identical increase of F_y (47%), indicating that adding the pos-tensioned anchors did not affect the load corresponding to the yield initiation of the tension steel bars. This result is consistent for FB4_BG_Phi10 and FB4_BG_Phi8, since despite having different layouts and sectional area of the anchors, both presented almost identical yield loads. Comparison of FB0_G and FB2_G shows an increase of 21% in F_y as a result of bonding two single-CFRP laminates to the SHCC plate. The average increase for HCP$^{(L)}$ with four CFRP laminates was 35%. Despite this increase in F_y, there was only a marginal increase in the corresponding deflection, δ_y, of the HCP$^{(L)}$ strengthened beams when compared to FB_R.

3.1.2.3. Ultimate Load and Corresponding Deflection

The ultimate load, F_u, for beams with a smooth degradation in their post-peak phase (beams FB_R and FB0_G), is defined as the point where the decrease in maximum registered load reaches 15%, unless the concrete crushing is predominant. In the other hand, for the beams with a sudden drop just beyond the peak load, the ultimate and maximum loads, F_m, coincide. According to the above mentioned criteria, the ultimate load, F_u, of FB0_G (61.03 kN) was almost the same as FB_R (61.8 kN), but occurred in a 12% higher ultimate deflection, δ_u. Attaching HCP$^{(L)}$ to the tension face of the beam by means of only anchors (beam FB2_B) resulted in an increase of 72% in ultimate load, F_u, when compared to the one registered for the reference beam (FB_R). At this ultimate load, the strain gauge "PM" registered a strain level of 1.19% in the CFRP laminates. In the other words, 74% of the potential tensile strength of the HCP$^{(L)}$ was mobilized by this attaching layout. The mid-span deflection at the ultimate load, δ_u, of FB2_B was 37.5 mm, which is 36% lower than the corresponding deflection of the FB_R beam.

When epoxy adhesive was used instead of chemical anchors to attach the HCP$^{(L)}$ (beam FB2_G), the ultimate load, F_u, was further increased in 13%. A higher tensile stress of CFRP laminates was therefore mobilized, to the extent that the strain at "PM" was 12% higher than the corresponding value in beam FB2_B. The beam FB2_G reached a δ_u of 25.9 mm, which was 56% and 31% lower than the corresponding deflection of FB_R and FB2_B, respectively. The reduction in deflection at the ultimate load of FB2_G regarding to FB2_B is attributed to a restricted sliding at the interface of HCP$^{(L)}$ and beam. Finally, the combination of chemical anchors and epoxy adhesive, for fixing HCP$^{(L)}$ to the FB2_BG beam, assured the full strengthening potential of HCP$^{(L)}$, providing to this beam an ultimate load and deflection of 128 kN and 32.8 mm, respectively. This ultimate load was 107% larger than the corresponding load obtained by FB_R. The HCP$^{(L)}$ reached its strengthening capacity, since the CFRP laminates have ruptured in the pure bending zone, close to the loaded section at the right side of the beam (see Figure 9). It is worth to mention that the first series of horizontal cracks in concrete cover corresponding to the detachment progress was observed at a load level of 122 kN, which is very close to the ultimate load of FB2_G (120 kN). However, due to an effective functioning of the anchors, despite initiation of detachment through the concrete cover and its propagation towards the end of the HCP$^{(L)}$ (see Figure 9a), the tensile resistance of CFRP laminates was fully exploited. Considering the maximum load obtained for FB2_BG, a flexural capacity of 51.2 kN·m

was achieved, which is 12% higher than the predicted values based on the analytical solutions. The ultimate deflection, δ_u, of FB2_BG was 32.8 mm, being 26.7% higher than the corresponding value of FB2_G, but 44% lower than the deflection registered at the ultimate load of FB_R. The onset of detachment of HCP$^{(L)}$ of FB4_BG_Phi10 was at a load level of 134 kN, when a horizontal crack, originated from an existing flexural-shear crack at the vicinity of the loaded section at the right shear span of the beam, has progressed. However, due to the resisting contribution of the anchors, the detachment progress was delayed and an ultimate load of 153.2 kN was attained. For this load level a strain of 1.25% at the mid-length of the CFRP laminates was measured by "PM", which is 78% of ultimate tensile strain of the CFRP laminates. The mid-span deflection of FB4_BG_Phi10 at the occurrence of maximum load was 27.7 mm, 53% lower than the corresponding value for FB_R. Initiation of detachment of HCP$^{(L)}$ of FB4_BG_Phi8 has occurred at load level of 137 kN, which is slightly higher than the corresponding load in FB4_BG_Phi10. This indicated that a staggered configuration of the anchors resulted in a greater distribution of the tensile stress along the width of the strengthening plate [23] and reduced the shear-lag mechanism associated with using a single row of anchors [24]. As a result, a more uniform interfacial stress distribution along the concrete cover was expected. Consequently, an ultimate load carrying capacity, F_u, of 165 kN was attained, being 167% and 8% higher than the corresponding values for FB_R and FB4_BG_Phi10, respectively. For this load level a strain value of 1.33% was measured by the strain gauge "PM", corresponding to mobilization of 83% of CFRP laminates' tensile strain capacity. The flexural capacity of the FB4_BG_Phi8 beam was 66.1 kN·m, almost the same predicted by the analytical approach at the rupture of CFRP laminate, and assuming simplified elastic-perfectly plastic responses for the SHCC and steel bars. The mid-span deflection of FB4_BG_Phi8 at the occurrence of the ultimate load was 49% lower than the corresponding one of the FB_R, but slightly higher than the registered value in the FB4_BG_Phi10.

3.1.2.4. Ductility

As a general trend, in comparison with FB_R, attaching HCP$^{(L)}$ to the beam's soffit reduced the deflection corresponding to the ultimate load, δ_u, while a marginal change in the mid-span deflection corresponding to the yield of tension steel bars, δ_y, can be observed. As it was discussed in the previous section, in comparison with the results registered in the FB_R beam, the minimum and the maximum reduction in δ_u was 36% and 56%, and have occurred in the FB2_B and FB2_BG beams, respectively. As

a consequence of this reduction, the deflection ductility, ($\mu_\delta = \delta_\mathrm{u}/\delta_\mathrm{y}$), of the strengthened beams was lower than that obtained in the reference beam (FB_R). However, still a lower bound of 3.6 for displacement ductility (beam FB4_BG_Phi10) was achieved. Moreover, all the strengthened beams presented an adequate ductility considering the specifications of ACI 440.2R-08 [25]. According to this specification, an RC beam flexural strengthened with a FRP bonded system has enough ductility if the strain in steel reinforcement at the failure of beam is greater than 0.005 mm/mm. Considering the strain levels recorded in the CFRP laminates of all of the strengthened beams, it can be concluded that the strain in tension steel bars were higher than 0.5% (see section 4.2.). Finally, comparing the ductility values obtained in FB2_BG and FB4_BG_Phi8 beams, and taking into account that detachment of HCP$^{(L)}$ was the governing failure mode in the FB4_BG_Phi8, it can be concluded that a double amount of CFRP laminates in the structure of the HCP$^{(L)}$ had a relatively low adverse effect in μ_δ, a reduction of about 11.5%.

3.1.2.5. Serviceability Limit States

To verify the cracking status on both the strengthening layer and the lateral faces of the beams, there was a pause in the loading procedure at a 10 mm displacement measured by the internal LVDT of the jack. This measured deflection by the internal LVDT of the beam corresponds to a beam's mid-span deflection between 8.1 and 8.9 mm registered by the middle LVDT supported on the Japanese Yoke. This deflection was selected in compliance with a deflection equal to a clear-span divided by 250 $\left(\delta_{250} = \frac{L_S}{250}\right)$, which is recommended as a service limit deflection by EC2 [21]. Except in the case of FB0_G, there was no crack visible to the naked eye on the surface of the strengthening layer, while several cracks along the loading span at lateral faces of the beams already existed. In the case of FB0_G, at this deflection level, a crack was already localized in the SHCC plate and was wide enough to be visible at one of the loaded sections. According to the recommendations of ACI 440.2R-08 [25], for externally FRP-bonded flexurally strengthened RC beams, to avoid inelastic deformations, the yielding of existing steel bars under service load should be prevented. Therefore, the stress in the existing steel bars under service load should be limited to 80% of the yield stress. This stress reduction limit takes into account the stress increase in the steel bars due to effects of long-term loadings such as creep, shrinkage and cyclic fatigue. It also includes the statistical uncertainty level on the yield stress of the steel bars. Obviously at this service load, the deflections of all the strengthened beams are far below δ_{250}.

If the specifications of Portuguese design code between 60's and 80's are considered, deflection of the beams at service load, F_{400}, should be limited to the beam's span divided by 400, $\left(\delta_{400} = \frac{L_S}{400}\right)$. According to this criterion, the service load, F_{400}, of the beams of group II has more than 53% increase comparing to that of the reference beam. This increase for beams of group I with a continuous bond between HCP$^{(L)}$ and RC was higher than 41%. When a discrete connection of HCP$^{(L)}$ to RC beam was used, the case of FB2_B, this increase was much lower (22%). It should be noted that bonding only a SHCC plate of 20 mm thickness (beam FB0_G) resulted in 31% increase in F_{400}, however, only a marginal safety to the yield load, F_y, exists (5.7%). This safety margin in the case of the beams of group II was higher than 22%.

3.1.2.6. Strain Profile along the CFRP Laminates

Figure 11 represents the strain profile in CFRP laminates along the HCP$^{(L)}$ at different load levels for FB2_G and FB4_BG_Phi10. Positions of the strain gauges are measured from beam's right support, where the failure occurred. In these figures, strain profiles at the load corresponding to the yield of tension steel bars, the onset of detachment of HCP$^{(L)}$, and the maximum load are denoted by "Y", "D" and "M", respectively. For both of these beams, at the onset of detachment of concrete cover, a sudden increase in the strain measured under the loaded section, and similarly in the strain measured at the mid-span, can be recognized. The strain values corresponding to the onset of detachment, as measured by the strain gauge "PL", were 0.9% and 0.97% for FB2_G and FB4_BG_Phi10, respectively. A larger strain value measured for FB4_BG_Phi10 can be attributed to the effect of pos-tensioning force in chemical anchors, which in turn resulted in confining of the concrete cover. Therefore, it can be concluded that the strain corresponding to detachment of HCP$^{(L)}$ is independent of the number of CFRP laminates in its structure. The role of chemical anchors in delaying the detachment progress is obvious when strain values measured at "PTC" for these two beams are compared. In fact, in FB2_G further loading beyond the onset of detachment of HCP$^{(L)}$ resulted in a high increase in the strain measured by "PTC", while the corresponding strain value in FB4_BG_Phi10 had a gradual increase up to a load level very close to the failure of this beam.

4. Numerical Modelling

Several studies showed that a layered-section model can be used to predict moment-curvature $(M - \chi)$ of composite sections, which can be employed in a numerical strategy to estimate the load-deflection of the elements failing in bending, with enough accuracy compared to the experimental results [26, 27]. According

to this strategy, a cross-section is discretized into several thin layers (see Figure 12). Based on the assumption that plane sections remain plane after bending, for a gradual increase in curvature of the cross-section the state of the strain at the middle of each layer is determined. Then, for each state of the strain, the stress values can be obtained using the constitutive law of the corresponding material of each layer. Since the distribution of the stress along the depth of the cross-section is already determined, the state of the static equilibrium can be checked and then established, if needed, through an iterative solution by adjusting the depth of the neutral axis. When the stress distribution accomplishes the state of equilibrium of the section, the bending moment (M) for that corresponding curvature (χ) is calculated. According to this strategy, and following the algorithm presented in [27], a VBA was implemented into an excel file to calculate the moment-curvature of a flexurally strengthened cross-section. The source of this code can be found in [9]. The evolution of the moment-curvature $(M-\chi)$ can be used in a numerical model to estimate the load-deflection of a simply supported beam, discretized into Euler-Bernoulli elements. In this method, for each load increment, ΔF^q, the bending moment at the centroid of each element, M_e^q, is calculated. Afterwards, tangential flexural rigidity of each element, $(EI)_{Te}^q$, is evaluated from the element's $M-\chi$. The tangential stiffness matrix of each element, $\underline{K}_{Te}^q$, is then calculated using $(EI)_{Te}^q$. By assembling tangential stiffness of each element, the tangential stiffness of the beam, $\underline{K}_{TE}^q$, is obtained. Finally, by solving the system of linear equations, $\underline{K}_{TE}^q \Delta \underline{u}^q = \Delta \underline{F}^q$, the increment in nodal displacements, $\Delta \underline{u}^q$, is obtained and the matrix of nodal displacements, $\underline{u}^q = \underline{u}^{q-1} + \Delta \underline{u}^q$, will be updated. This approach is detailed in [27].

4.1. Constitutive Laws of the Materials

As depicted in Figure 13a, the tensile behaviour of SHCC is modelled assuming an elastic-linear stress-strain response up to the formation of the first crack. The post-cracking response of SHCC is simulated using a linear ascending branch corresponding to the tensile strain hardening phase. Following this hardening branch, the reduction in stress is taken into account adopting a bi-linear regime up to a zero stress state. The elastic modulus (E_{sh}), the stress at the first crack (f_{sh}^{cr}), the tensile strength (f_{sh}^{u}) and the tensile strain hardening capacity (ε_{sh}^{u}) are introduced based on the average results of direct tensile tests and parameters for the softening regime are adopted from [28]. Values of the parameters used to define the tensile stress-strain relationship of the SHCC are reported in Table 4. In compliance with the results of

tensile tests, the stress-strain response of CFRP laminates is considered linear-elastic with a maximum tensile strain corresponding to the average strain obtained at the rupture of laminates. The uniaxial stress-strain relationship for the steel bars is based on the proposed model by Park and Paulay [29], represented schematically in Figure 13b and mathematically in equations (47) to (49). Steel bars are assumed to behave similarly under monotonic compression and tension loadings.

$$f_{st} = f_{st}^{y}\left[\frac{m(\varepsilon_{st}-\varepsilon_{st}^{sh})+2}{60(\varepsilon_{st}-\varepsilon_{st}^{sh})+2}+\frac{(\varepsilon_{st}-\varepsilon_{st}^{sh})(60-m)}{2(30r+1)^2}\right] \qquad \varepsilon_{st}^{sh} < \varepsilon_{st} \tag{47}$$

where,

$$r = \varepsilon_{st}^{u} - \varepsilon_{st}^{sh} \tag{48}$$

$$m = \frac{(f_{st}^{u}/f_{st}^{y})(30r+1)^2 - 60r - 1}{15r^2} \tag{49}$$

Concrete in compression is formulated using the Mander model [30], see Figure 14a and equations (50) to (54). With the exception of the strain corresponding to the maximum compressive strength (ε_{cc}^{m}), which is calculated using the recommendations of EC2 [21] and indicated in equation (54), the other parameters of this model are taken from the results of uniaxial compression tests. Table 6 reports values of the parameters adopted to define the constitutive law of concrete under compression.

$$f_{cc} = \frac{\kappa\alpha f_{cc}^{m}}{\alpha - 1 + \kappa^{\alpha}} \qquad \varepsilon_{cc} \leq 2\varepsilon_{cc}^{m} \tag{50}$$

$$f_{cc} = \left(\frac{2\alpha f_{cc}^{m}}{\alpha - 1 + 2^{\alpha}}\right)\left(\frac{\varepsilon_{cc}^{f} - \varepsilon_{cc}}{\varepsilon_{cc}^{f} - 2\varepsilon_{cc}^{m}}\right) \qquad 2\varepsilon_{cc}^{m} < \varepsilon_{cc} \leq \varepsilon_{cc}^{f} \tag{51}$$

where,

$$\kappa = \varepsilon_{cc}/\varepsilon_{cc}^{m} \tag{52}$$

$$\alpha = \frac{E_c}{E_c - (f_{cc}^{m}/\varepsilon_{cc}^{m})} \tag{53}$$

$$\varepsilon_{cc}^{m} = 0.07\ (f_{cc}^{m})^{0.31} \quad \leq 2.8\ (\%) \qquad [21] \tag{54}$$

Tensile behaviour of concrete is simulated by a linear-elastic phase, followed by a post-cracking regime. Concrete tensile strength (f_{ct}^{cr}) is calculated using the specifications of EC2 [21], indicated in equation (55). To address interaction between steel bars and the surrounding concrete in numerical simulation, a multi-linear tension-stiffening model that takes into account the contribution of concrete up to the ultimate strength of reinforcement [31]is employed. The effective concrete embedment-zone is defined as an area of concrete around the centre of the bar with a width and depth equal to 15 times the steel bar diameter [32]. For other parts of concrete, a tension-softening model [32] represented in Figure 13b is adopted.

$$f_{ct}^{cr} = 0.3\ (f_{cc}^{m} - 8)^{2/3} \tag{55}$$

To calibrate parameters of the tension-stiffening model, the evolution of tensile strain in longitudinal steel bar of FB_R and in longitudinal CFRP laminate of FB2_BG, versus bending moment obtained from fibre-section analysis are compared to those obtained in experimental tests. Hence, employing an inverse analysis, the parameters of the tension-stiffening model were adjusted to obtain the best match between the aforementioned results (strain *versus* moment from numerical and experimental studies).

4.2. Numerical versus Experimental Results

Figure 15a and Figure 15b compare strain *versus* moment obtained from layer-section model analysis with the corresponding one from experimental test (strain values registered at the mid-length of the specified longitudinal reinforcement of FB_R and FB2_BG). The strain *versus* moment obtained for FB4_BG_Phi8 is also presented in Figure 15c, that confirms the accuracy of the tension-stiffening model for the beams flexurally strengthened by HCP$^{(L)}$. Values for the parameters of the tension-stiffening law, which resulted in the most fitted strain *versus* moment curve of the numerical model to the experimental tests, are indicated in Table 7. Values for the parameters of the tension-softening model were adopted from [32] and are also reported in the same table.

Figure 15b and Figure 15c also indicate the strain evolution in the steel bars of beams FB2 and FB4, respectively, obtained from the numerical strategy. According to these data, the strain values in longitudinal steel bars FB2 and FB4 are 1.42% and 1.16%, respectively. As discussed in section 3.1.2.4, these values

are much higher than 0.005 mm/mm, which is one of the requisites in an FRP-bonded flexurally strengthened RC beam in order to be recognized as a ductile section [25].

Load-deflection responses obtained from experimental test and numerical model of each beam are represented in Figure 16. In general, a good agreement between numerical and experimental results can be observed. The model was capable of predicting with enough accuracy the load and deflection at the formation of the first crack, and also the corresponding values at the onset of yield of tension steel bars. A slightly higher post-cracking and post-yielding stiffness presented by numerical simulation is attributed to the fact that the numerical strategy follows the Euler-Bernoulli theory to calculate the deflection in each element of the beam, which in turn eliminates the stiffness reduction due to the flexural-shear cracking or shear cracking along the beam's span. Moreover, following a perfect bond assumption, the sliding at the interface of the CFRP-laminates and the surrounding SHCC, and also between the $HCP^{(L)}$ and the beam's soffit, is not taken into account, while the detachment progress was observed in all $HCP^{(L)}$ strengthened beams. Thus, a higher post-yield stiffness and a lower ultimate deflection predicted by the adopted numerical strategy were expected.

5. Conclusions

The present work was, mainly, dedicated to the experimental assessment of a Hybrid Composite Plate (HCP) for the flexural strengthening of RC beams. An analytical model approach is proposed for predicting the load-deflection response of these beams. From the main obtained results the following relevant conclusions can be pointed out:

- In comparison with the results of the reference beam, all of the adopted strengthening schemes resulted in a superior response in terms of the load and deflection at the onset of cracking, yield load of the tension steel bars, and ultimate load.
- The deflection ductility of all the $HCP^{(L)}$ strengthened beams, compared to the reference beam, was decreased. However, a satisfactory lower bound of 3.6 for deflection ductility at a 153% increase in the ultimate load was preserved. The largest deflection ductility of the $HCP^{(L)}$ strengthened beams was 5.3, corresponding to the strengthening solution based on $HCP^{(L)}$ fixed to the RC beam by means of only chemical anchors.

- When a combination of epoxy adhesive and chemical anchors was used to attach $HCP^{(L)}$ to the beam's soffit, the full strengthening potential of $HCP^{(L)}$ containing two CFRP laminates at a satisfactory deflection ductility of 4.4 was mobilized.
- A staggered configuration of the anchors delayed the progress of detachment in concrete cover, as compared to the configuration that incorporates a layout of one row of anchors. Hence, comparing to the latter connection configuration, both higher flexural capacity and deflection ductility with the staggered layout of anchors can be achieved. Using this configuration of anchors in combination with epoxy adhesive, a significant increase in load carrying capacity (167%, compared to the reference beam), with a satisfactory deflection ductility of about 4.0 was attained. For this strengthening configuration, up to 83% of the potential strengthening of $HCP^{(L)}$ was mobilized.
- The detachment in NSM-CFRP strengthened RC beams often involves fracture and disintegration of the concrete surrounding the bonded strips. However, none of the $HCP^{(L)}$ strengthened beams had any sign of such failure at the SHCC around the CFRP laminates. This indicates how the fibre reinforcement mechanisms of arresting micro-cracks in a strain hardening composite prevents the formation of the macro-cracks and contribute for the maintenance of the integrity of the $HCP^{(L)}$ up to the development of high tensile strain in CFRP laminates.
- Based on a simplified concrete compressive block and assuming a full composite action, the analytical formulation predicted the ultimate moment capacity of the beam, failed by CFRP rupture, with a 12% tolerance.
- The adopted numerical strategy, based on a section-layer model, has predicted with satisfactory agreement, the general load-deflection response of both the reference beam and the strengthened ones (FB_R, FB0_G, FB2_BG) tested experimentally. However, for the cases where concrete cover detachment is a prevailing failure mode (FB4_BG), to predict the load-deflection response with a higher precision, further investigations are required for a better simulation of the local phenomena associated to the action of the anchors in a modified

numerical approach (e.g. identifying criteria for the detachment initiation, the detachment progress, and the occurrence of different failure modes in the $HCP^{(L)}$).

6. Acknowledgements

The study presented in this paper is a part of the research project titled "PrePam –Pre-fabricated thin panels by using advanced materials for structural rehabilitation" with reference number of PTDC/ECM/114511/2009. The first author acknowledges the Ph.D. scholarship SFRH/BD/65663/2009 provided by FCT. The authors also thank the collaboration of the following material suppliers: SIKA, Dow Chemical Co., ENDESA Compostilla Power Station, S&P and Hilti.

7. References

[1] Teng J, Chen J, Smith ST, Lam L. Behaviour and strength of FRP-strengthened RC structures: a state-of-the-art review. Proceedings of the ICE-Structures and Buildings. 2003;156(1):51-62.

[2] Kachlakev D, McCurry DD. Behavior of full-scale reinforced concrete beams retrofitted for shear and flexural with FRP laminates. Compos Part B Eng. 2000;31(6–7):445-52.

[3] De Lorenzis L, Teng JG. Near-surface mounted FRP reinforcement: An emerging technique for strengthening structures. Compos Part B Eng. 2007;38(2):119-43.

[4] Shrestha J, Ueda T, Zhang D. Durability of FRP Concrete Bonds and Its Constituent Properties under the Influence of Moisture Conditions. J Mater Civ Eng. (SPECIAL ISSUE):A4014009.

[5] Burke PJ, Bisby LA, Green MF. Effects of elevated temperature on near surface mounted and externally bonded FRP strengthening systems for concrete. Cem Concr Compos. 2013;35(1):190-9.

[6] Benmokrane B, Mohamed HM. Durability Issues of FRP for Civil Infrastructure. In: Proceedings of 11th International Symposium on Fiber Reinforced Polymers for Reinforced Concrete Structures (FRPRCS11). Guimaraes, Conference June 26-28, Conference 2013. p. 11-4.

[7] Brena SF, Bramblett RM, Wood SL, Kreger ME. Increasing Flexural Capacity of Reinforced Concrete Beams Using Carbon Fiber-Reinforced Polymer Composites. ACI Struct J. 2003;100(1).

[8] Grelle SV, Sneed LH. Review of anchorage systems for externally bonded FRP laminates. Int J Concr Struct Mater. 2013;7(1):17-33.

[9] Esmaeeli E. Development of Hybrid Composite Plate (HCP) for the strengthening and increasing the energy dissipation capacity of RC members [Doctoral thesis]. Guimaraes: Univeristy of Minho; (to be Published in 2015).

[10] Esmaeeli E, Barros JAO, Sena-Cruz J, Fasan L, Li Prizzi FR, Melo J, et al. Retrofitting of interior RC beam–column joints using CFRP strengthened SHCC: Cast-in-place solution. Compos Struct. 2015;122:456-67.

[11] Esmaeeli E, Barros JAO, Baghi H, Sena-Cruz J. Development of Hybrid Composite Plate (HCP) for the Repair and Strengthening of RC Elements. 3rd International RILEM Conference on Strain Hardening Cementitious Composites (SHCC3-Delft). Dordrecht, Netherlands: RILEM Publications SARL; 2014.

[12] Esmaeeli E, Barros JAO, Baghi H. Hybrid Composite Plates (HCP) for Shear Strengthening of RC Beams. In: Proceedings of 11th International Symposium on Fiber Reinforced Polymers for Reinforced Concrete Structures (FRPRCS11). Guimaraes, Conference June 26-28, Conference 2013.

[13] Esmaeeli E, Barros JAO, Sena-Cruz J, Varum H, Melo J. Assessment of the efficiency of prefabricated hybrid composite plates (HCPs) for retrofitting of damaged interior RC beam–column joints. Compos Struct. 2015;119:24-37.

[14] Esmaeeli E, Barros J, Mastali M. Effects of curing conditions on crack bridging response of PVA reinforced cementitious matrix. In: Proceedings of 8th RILEM international symposium on fibre reinforced concrete: challenges and opportunities (BEFIB2012). Guimaraes, Portugal, Conference, Conference 2012.

[15] Esmaeeli E, Barros JAO, Baghi H. Hybrid Composite Plates (HCP) for Shear Strengthening of RC Beams. In: Proceedings of 11th International Symposium on Fiber Reinforced Polymers for Reinforced Concrete Structures (FRPRCS11). Guimaraes, Conference June 26-28, Conference 2013. p. 11-4.

[16] International Organization for Standardization – ISO 527-2:2012. Plastics — Determination of tensile properties — Part 2: Test conditions for moulding and extrusion plastics. Genève, Switzerland.

[17] International Organization for Standardization – ISO 527-5:2009. Plastics – Determination of tensile properties – Part 5: Test conditions for unidirectional fibre-reinforced plastic composites. Genève, Switzerland.

[18] LNEC E397-1993:1993. Concrete - Determination of the elasticity modulus under compression. Portuguese specification from LNEC.

[19] BS EN 12390-3:2009. Testing hardened concrete. Compressive strength of test specimens.

[20] BS EN ISO 15630-1:2010. Steel for the reinforcement and prestressing of concrete. Test methods. Reinforcing bars, wire rod and wire.

[21] EN1992-1-1. Eurocode 2: Design of Concrete Structures. Part 1-1: General Rules and Rules for Buildings. Brussels, Belgium: European Committee for Standardization; 2004.

[22] Teng JG, Smith ST, Yao J, Chen JF. Intermediate crack-induced debonding in RC beams and slabs. Constr Build Mater. 2003;17(6–7):447-62.

[23] Martin J, Lamanna A. Performance of Mechanically Fastened FRP Strengthened Concrete Beams in Flexure. J Compos Constr. 2008;12(3):257-65.

[24] Rizzo A, Galati N, Nanni A. Strengthening of off-system bridges with mechanically fastened pre-cured FRP laminates. ACI Special Publication. 2005;230.

[25] ACI. 440.2R-08 Guide for the Design and Construction of Externally Bonded FRP Systems for Strengthening Concrete Structures: ACI; 2008.

[26] El-Tawil S, Ogunc C, Okeil A, Shahawy M. Static and Fatigue Analyses of RC Beams Strengthened with CFRP Laminates. J Compos Constr. 2001;5(4):258-67.

[27] Barros JAO, Fortes AS. Flexural strengthening of concrete beams with CFRP laminates bonded into slits. Cem Concr Compos. 2005;27(4):471-80.

[28] Esmaeeli E, Manning E, Barros JAO. Strain Hardening Fibre Reinforced Cement Composites for the Flexural Strengthening of Masonry Elements of Ancient Structures. Constr Build Mater. 2013;38(SPECIAL ISSUE):1010-21.

[29] Park R. Reinforced concrete structures: John Wiley & Sons; 1975.

[30] Mander J, Priestley M, Park R. Theoretical Stress-Strain Model for Confined Concrete. J Struct Eng. 1988;114(8):1804-26.

[31] Wanser J, Sigrist V. Accounting for Tension Stiffening in Finite Element Modelling. In: Proceedings of 8th fib International PhD Symposium in Civil Engineering. Department of Civil Engineering, Technical University of Denmark, Conference 20 - 23 June, Conference 2010.

[32] Massicotte B, Elwi AE, MacGregor JG. Tension-stiffening model for planar reinforced concrete members. J Struct Eng. 1990;116(11):3039-58.

Figure Captions

Figure 1- Schematic presentation of tensile behaviour of CFRP and SHCC, crack propagation and crack width in SHCC at different loading stages, and crack propagation close to the rupture of CFRP at HCP (see list of notations for description of the adopted symbols)

Figure 2- Geometry and steel reinforcement arrangements of the representative beam of the experimental program (dimensions in mm)

Figure 3- Details of the strengthened beams (dimensions in mm)

Figure 4- Details of configuration of CFRP laminates bonded into the grooves of $HCP^{(L)}$ (a) single-CFRP laminate, and (b) double-CFRP laminate (dimensions in mm)

Figure 5- Four point bending test setup (dimensions in mm)

Figure 6- Schematic presentation of internal strain and stress distribution for a $HCP^{(L)}$ strengthened RC section at ultimate state (a) section configuration, (b) strain distribution, (c) simplified stress profile using equivalent concrete compressive rectangular block, (d) stress profile based on concrete parabolic compressive stress-strain curve (see notation list for the physical meaning of each symbol)

Figure 7- Load-deflection curves of the beams obtained from four point bending tests

Figure 8- Propagated damages at the end of the test of (a) FB2_B (bottom view), and (b) FB2_G

Figure 9- Propagated damages at the end of the test of FB2_BG, (a) front view, and (b) bottom view

Figure 10- Propagated damages at the end of the test of FB4_BG_Phi8, (a) front view, and (b) bottom view

Figure 11- Strain profile in CFRP laminate along the length of the beam at different load levels, with the distance measured from the right support, for (a) FB2_G, and (b) FB4_BG_Phi10, (in these figures superscripts “Y”, “D” and “M” denote the load at the yield of the tension steel bars, at the initiation of detachment, and at the maximum load, respectively).

Figure 12- Concept of Fibre-Section for the calculation of the moment-curvature of a composite section, (a) RC section, (b) RC section discretized into fibres, and (c) strain distribution at the middle-height of each fibre. (f_i, A_i and d_i are the stress, fiber area and depth at the middle of the fiber, respectively. F_R is the

residual force, unbalanced force, at the end of each iteration and M is the calculated moment for each given curvature (χ) .

Figure 13- Constitutive law to simulate tensile behaviour of (a) SHCC, and (b) steel reinforcement [29].

Figure 14- Adopted constitutive laws for concrete under (a) uniaxial compression [30], and under uniaxial tension, (b) for steel/FRP reinforced concrete (tension-stiffening in post-cracking), and (c) for plain concrete (tension-softening in post-cracking [32]) .

Figure 15- Comparison of the evolution of the mid-span strain in steel/CFRP reinforcement *versus* moment obtained from numerical and experimental studies in beam, (a) FB_R, (b) FB2_BG, and (c) FB4_BG_Phi8.

Figure 16- Comparison of the force-deflection curves obtained from numerical simulations with those of experimental tests.

Tables

Table 1- Details of beams and configurations of the strengthening plate

	Tension steel ratio (ρ)	Detail of HCP$^{(L)}$ / SHCC-Plate thickness (mm)	width (mm)	length (mm)	N	attaching technique
FB_R	0.35%	-	-	-	-	-
FB0_G		20	150	2000	0	Epoxy
FB2_B					2	Phi10(1)
FB2_G					2	Epoxy
FB2_BG					2	Phi10(1) + Epoxy
FB4_BG_Phi10					4	Phi10(1) + Epoxy
FB4_BG_Phi8					4	Phi8(2) + Epoxy

$\rho = A_{st}/bd_{st}$ where, A_{st} is the total area of tension steel bars, b is the width and d_{st} is the effective depth of the beam's cross section.
Phi10(1): one row of chemical anchors of 10 mm diameter.
Phi8(2): two rows of chemical anchors of 8 mm diameter with a staggered configuration.
N is the number of CFRP laminates adopted in the structure of the HCP$^{(L)}$.

Table 2- Predicted flexural capacity (M_R) of beams of groups I and II based on either an equivalent compressive stress block (M_{R1}) or nonlinear distribution of compressive stresses (M_{R2}) and comparison of these two approaches.

M_{R1} (kN·m)		M_{R2} (kN·m)		$\frac{M_{R1}-M_{R2}}{M_{R2}}$ (%)	
Group I	Group II	Group I	Group II	Group I	Group II
45.9	66.5	45.7	66.2	0.44	0.45

Table 3- Results obtained from the analysis of the tested beams

beam	first crack		steel yield		ultimate		service	deflection ductility	strain gauge "PM"	failure mode[d]
	δ_{cr} (mm)	F_{cr} (kN)	δ_y (mm)	F_y (kN)	δ_u (mm)	F_u (kN)	F_{400} (kN)	μ_δ[b]	%	-
FB_R	0.31	21.5	7.1	59.3	58.4	61.8	51.8	8.2		SY-CC
	-	-	-	-	-	-	-	-	-	
FB0_G	0.53	33.3	6.1	71.8	65.3	61.03	67.9	10.7	-	SY-CC
	(71%)[a]	(55%)	(-14%)	(21%)	(12%)	(-1.2%)	(31%)	(30%)	-	
FB2_B	0.44	23.5	7.1	72.9	37.5	106.0	63.1	5.3	1.19	SH
	(42%)	(9%)	(0%)	(23%)	(-36%)	(72%)	(22%)	(-36%)	[74%][c]	
FB2_G	0.54	33.2	7.2	87	25.9	120.0	74.9	3.6	1.33	DH
	(74%)	(54%)	(1%)	(47%)	(-56%)	(94%)	(45%)	(-56%)	[83%]	
FB2_BG	0.57	34.5	7.5	87.3	32.8	128.1	73.1	4.4	1.58	RL
	(84%)	(60%)	(6%)	(47%)	(-44%)	(107%)	(41%)	(-47%)	[99%]	
FB4_BG_Phi10	0.60	32.2	7.6	96.8	27.7	153.2	79.1	3.6	1.25	DH
	(94%)	(50%)	(7%)	(63%)	(-53%)	(148%)	(53%)	(-56%)	[78%]	
FB4_BG_Phi8	0.62	34.7	7.7	97.6	30.0	165.2	79.8	3.9	1.33	DH
	(100%)	(61%)	(8%)	(65%)	(-49%)	(167%)	(54%)	(-53%)	[83%]	

a) Values in brackets () are the change of each measure regarding its corresponding value in FB_R beam.
b) Deflection ductility μ_δ is defined as δ_u/δ_y;
c) Values in brackets [ ] are the percentage ratio of the strain measured in CFRP laminate at the mid-span of the beam to the average strain obtained at the rupture of CFRP laminates in tensile tests.
d) Failure modes- Tension steel Yield followed by Concrete Crushing (SY-CC), Splitting of HCP$^{(L)}$ (SH), Detachment of HCP$^{(L)}$ (DH), Rupture of CFRP laminates of HCP$^{(L)}$ (RL).

Table 4- Values adopted for the parameters defining tensile constitutive law of SHCC

E_{sh} (MPa)	f_{sh}^{cr} (MPa)	f_{sh}^{u} (MPa)	ε_{sh}^{u} (%)	ζ	γ_1	γ_2
18420	2.5	3.75	1.54	0.11	5	9

Table 5- Values of the parameters defining constitutive law of the longitudinal steel bars

E_s (GPa)	ε_s^y (%)	f_s^y (MPa)	ε_s^{sh} (%)	f_s^{sh} (MPa)	ε_s^u (%)	f_s^u (MPa)
215.825	0.25	536	2.5	536	12	629

Table 6- Parameters defining constitutive law for concrete under compression

E_c (GPa)	f_c^m (MPa)	ε_c^m (%)	f_c^t (MPa)
32.52	31.26	0.2	2.45

Table 7- Parameters defining tensile post-cracking response of concrete

	φ	ξ_1	ξ_2	β_1	β_2	ψ_1	ψ_2	ψ_3
Plain concrete	0.33	5	16	-	-	-	-	-
Steel reinforced concrete				0.45	0.20	5.0	0.85	0.95
CFRP reinforced concrete				0.60	0.45	5.0	0.85	0.95

Notations

a	distance of resultant compressive force from neutral axis
b	width and depth of beam
h	depth of beam
A_f	section areas of CFRP laminates
A_f^b	balanced section area of CFRP laminates
A_{sc}	section area of the compression steel reinforcement
A_{st}	section area of the tension steel reinforcement
A_{sh}	section area of SHCC
E_c	modulus of elasticity of concrete
E_{sc}	modulus of elasticity of compression steel reinforcement
E_{sh}	modulus of elasticity of SHCC
E_f	modulus of elasticity of CFRP laminates
$(\mathrm{EI})_{\mathrm{Te}}^{\mathrm{q}}$	tangential flexural rigidity of each beam's element
d'	distance between the centroid of compression steel and the extreme concrete compressive fibre
d_f	distance between centroid of CFRP laminates and the extreme compressive fibre
d_{sh}	distance between centroid of SHCC and the extreme compressive fibre
d_{st}	distance between centroid of tension steel and the extreme compressive fibre
f_{cc}	compressive stress in concrete
f_{cc}^t	strain in the extreme compressive fibre of the concrete
f_{ct}	tensile stress in concrete
f_{ct}^{cr}	concrete uniaxial tensile strength (stress at tensile cracking)
f_{cc}^m	mean compressive strength of concrete cylinder
f_{cd}	design value of concrete compressive strength
f_f	stress in CFRP
f_f^r	rupture stress of CFRP
f_{sh}	stress in SHCC
f_{sc}^y	yield strength of compression steel bars

f_{sh}^{cr}	cracking strength of SHCC (tensile stress at the onset of first crack)
f_{sh}^{u}	ultimate tensile strength of SHCC
f_{st}	stress at tension steel bars
f_{st}^{y}	yield strength of tensile steel bars
f_{st}^{u}	ultimate (maximum) tensile strength of tension steel bars
F_{400}	service load at δ_{400}
F_{cc}	resultant force in compression concrete
F_{sc}	resultant force in compression steel bars
F_{st}	resultant force in tension steel bars
F_{sh}	resultant force in SHCC
F_{f}	resultant force in CFRP laminates
F_{cr}	load at the onset of flexural cracking in beam
F_{m}	peak (maximum) flexural load of the beam
F_{y}	flexural load corresponding to the yield of tension steel reinforcement
F_{u}	ultimate flexural load of the beam
$\underline{K}_{Te}^{q}$	tangential stiffness matrix of each beam's element
$\underline{K}_{TE}^{q}$	tangential stiffness of the beam
L_{s}	beam's supporting span
M	bending moment for a given curvature
M_{R}	maximum resisting bending moment
$\mathrm{M}_{\mathrm{e}}^{\mathrm{q}}$	bending moment at the centroid of each element after each $\Delta\mathrm{F}^{\mathrm{q}}$
n	depth of natural axis of beam's section
x	distance of a fibre from natural axis
ε_{cc}	compressive strain in concrete
ε_{cc}^{m}	strain corresponding to the concrete compressive strength
ε_{cc}^{t}	compressive strain in extreme fibre of concrete
ε_{cc}^{u}	ultimate concrete compressive strain
ε_{ct}	tensile strain in concrete

ε_{ct}^{cr}	strain at tensile strength of concrete (onset of cracking)
ε_f	strain in CFRP laminates
ε_f^r	rupture strain of CFRP laminates
ε_{sc}	strain at the compression steel reinforcement
ε_{sc}^y	strain corresponding to the yield of compression steel reinforcement
ε_{sh}	strain at the centroid of the SHCC
ε_{sh}^{cr}	strain at the first tensile crack in SHCC
ε_{sh}^u	strain at the ultimate tensile strength of SHCC
ε_{st}	strain in tension steel reinforcement
ε_{st}^y	strain corresponding to the yield of tension steel reinforcement
ε_{st}^{sh}	strain at the onset of pseud strain-hardening in the steel reinforcement
ε_{st}^u	strain corresponding to the tensile strength of the steel reinforcement
μ_δ	deflection ductility factor
δ_{250}	service limit deflection equal to beam's span divided by 250
δ_{400}	service limit deflection equal to beam's span divided by 400
δ_{cr}	deflection corresponding to the onset of flexural cracking
δ_y	deflection corresponding to the yield of steel reinforcement
δ_u	deflection corresponding to the ultimate load
χ	curvature of a beam's section
ΔF^q	load increment
$\Delta \underline{u}^q$	increment in deflection of the beam at each ΔF^q
$\underline{u}^q$	matrix of nodal displacements

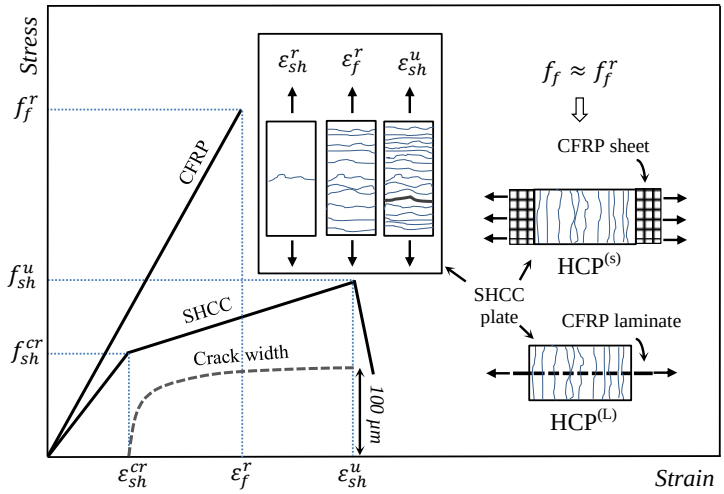

Figure 1- Schematic presentation of tensile behaviour of CFRP and SHCC, crack propagation and crack width in SHCC at different loading stages, and crack propagation close to the rupture of CFRP at HCP (see list of notations for description of the adopted symbols)

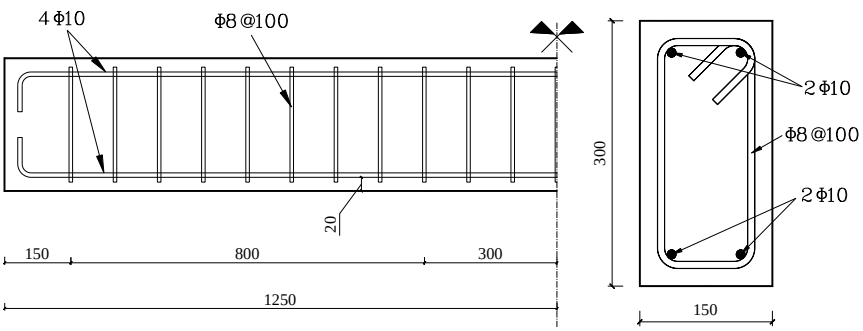

Figure 2- Geometry and steel reinforcement arrangements of the representative beam of the experimental program (dimensions in mm)

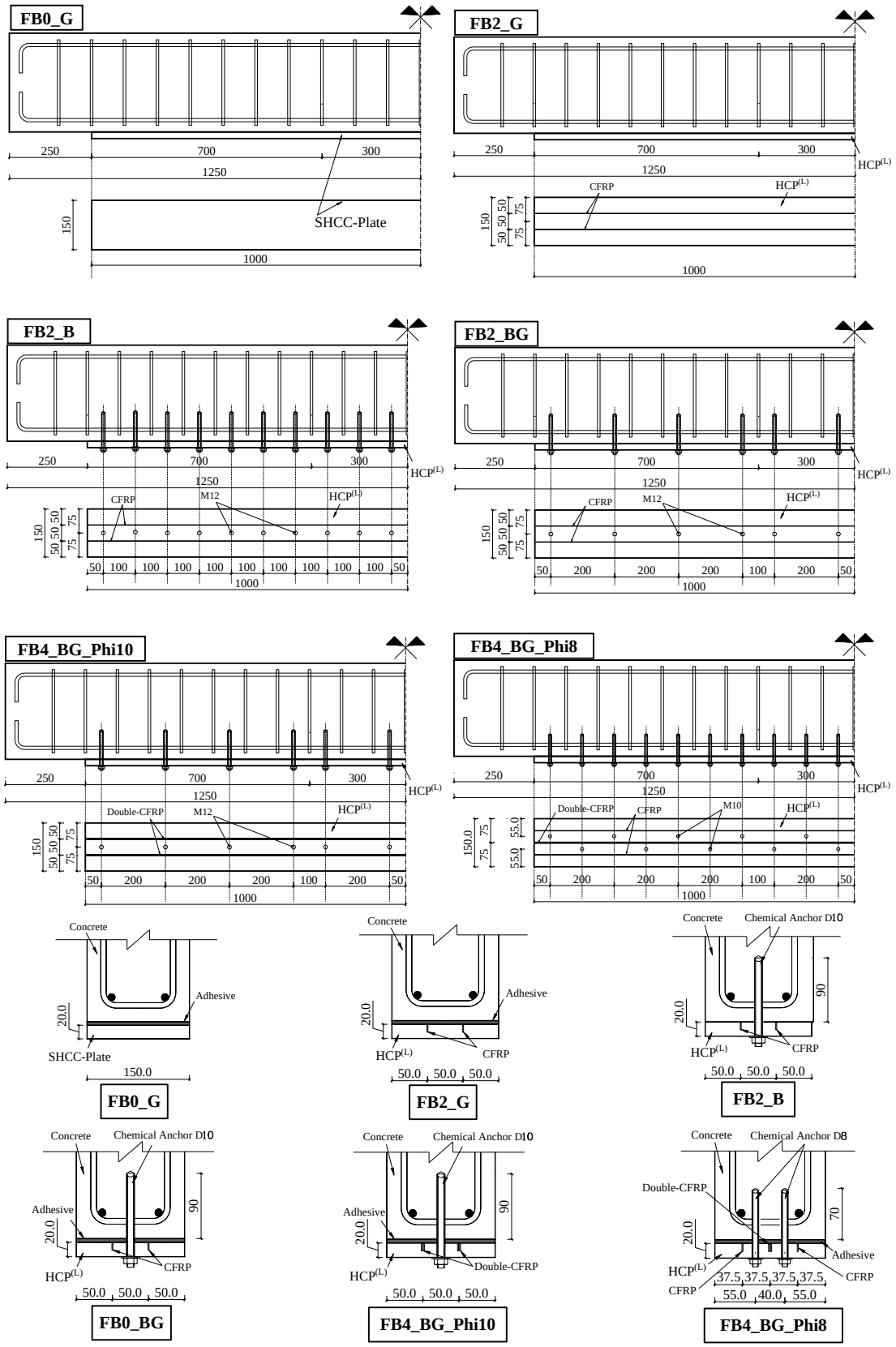

Figure 3- Details of the strengthened beams (dimensions in mm)

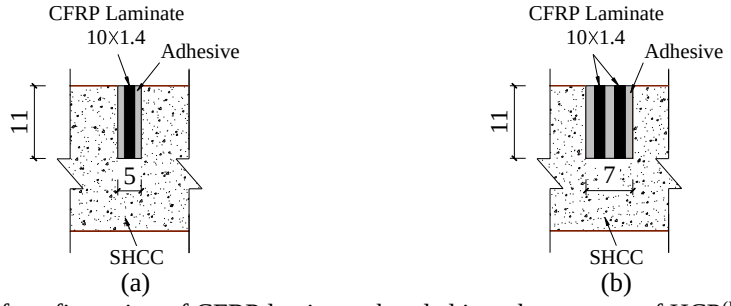

Figure 4- Details of configuration of CFRP laminates bonded into the grooves of HCP$^{(L)}$: (a) single-CFRP laminate, and (b) double-CFRP laminates (dimensions in mm)

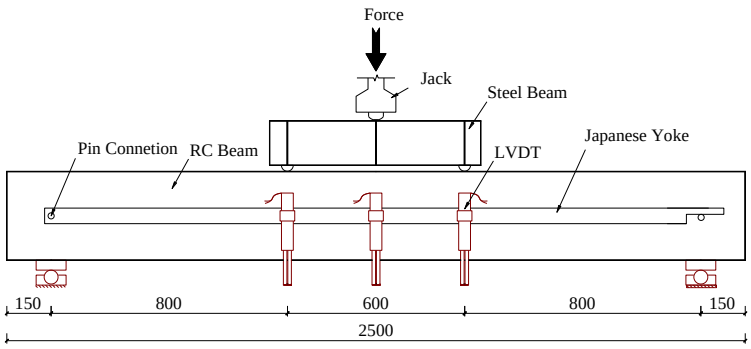

Figure 5- Four point bending test setup (dimensions in mm)

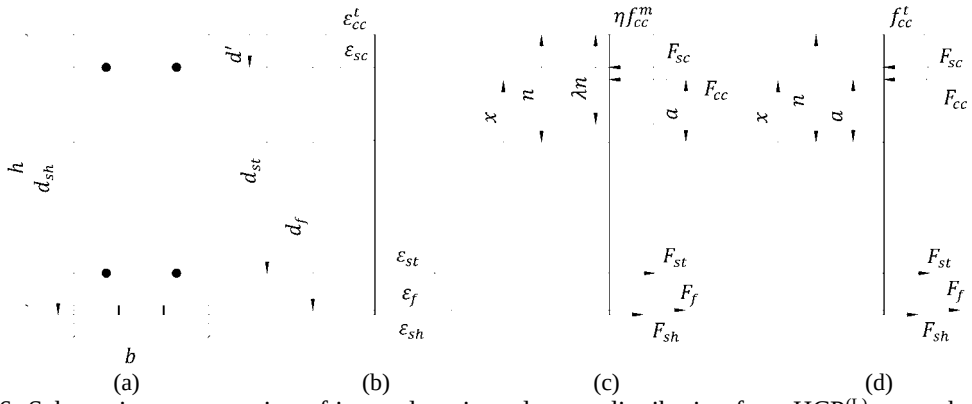

Figure 6- Schematic representation of internal strain and stress distribution for a HCP$^{(L)}$ strengthened RC section at ultimate state (a) section configuration, (b) strain distribution, (c) simplified stress profile using equivalent concrete compressive rectangular block, (d) stress profile based on concrete parabolic compressive stress-strain curve (see notation list for the physical meaning of each symbol)

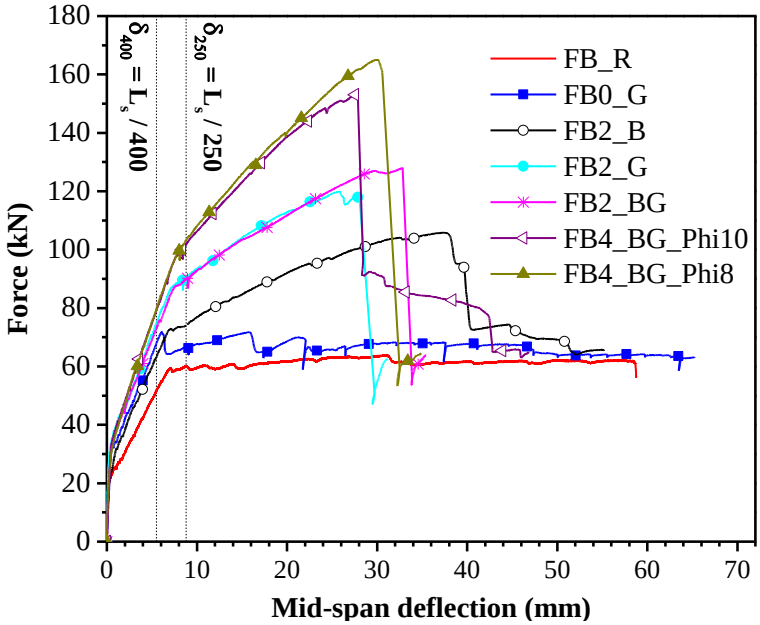

Figure 7- Load-deflection curves of the beams obtained from four point bending tests

(a) (b)

Figure 8- Propagated damages at the end of the test of (a) FB2_B (bottom view), and (b) FB2_G

(a) (b)

Figure 9- Propagated damages at the end of the test of FB2_BG, (a) front view, and (b) bottom view

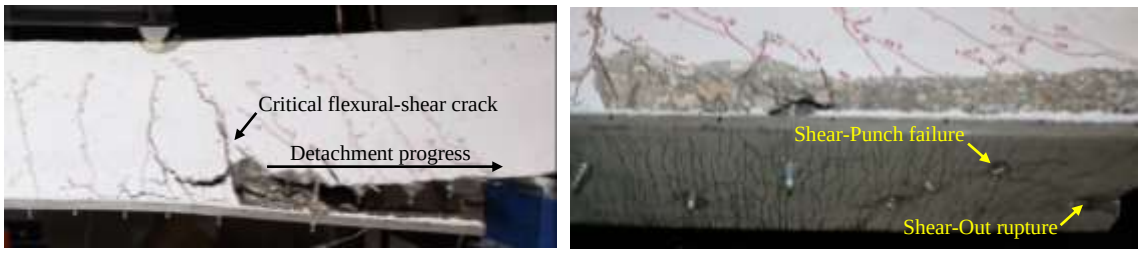

(a) (b)

Figure 10- Propagated damages at the end of the test of FB4_BG_Phi8, (a) front view, and (b) bottom view

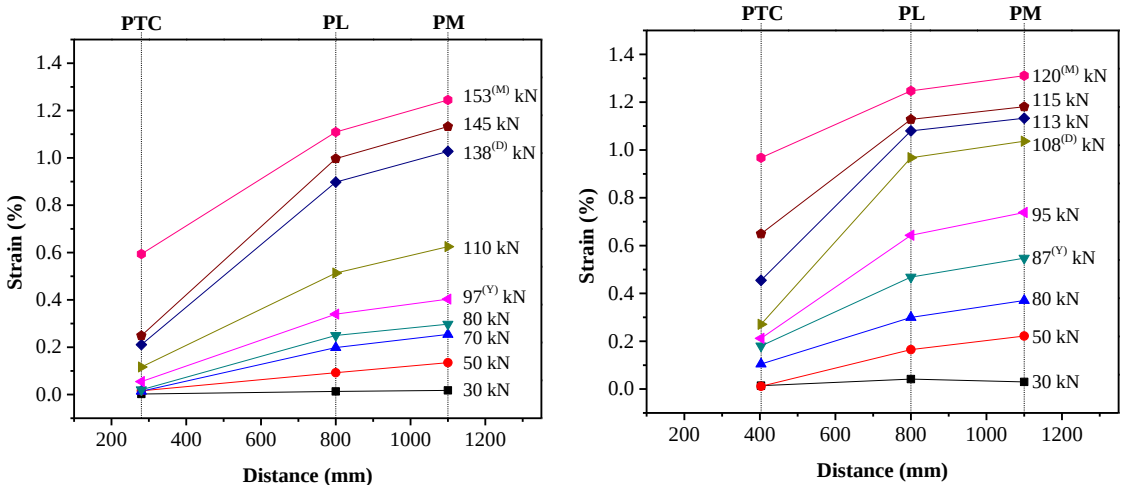

(a) (b)

Figure 11- Strain profile in CFRP laminate along the length of the beam at different load levels, with the distance measured from the right support, for (a) FB2_G, and (b) FB4_BG_Phi10, (in these figures superscripts "Y", "D" and "M" denote the load at the yield of the tension steel bars, at the initiation of detachment, and at the maximum load, respectively).

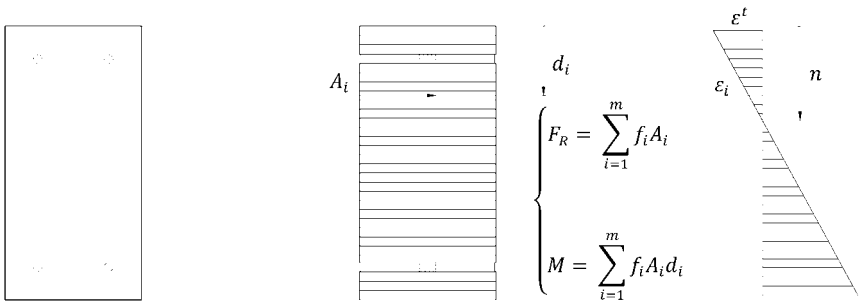

(a) (b) (c)

Figure 12- Concept of Fibre-Section for the calculation of the moment-curvature of a composite section, (a) RC section, (b) RC section discretized into fibres, and (c) strain distribution at the middle-height of each fibre. (f_i, A_i and d_i are the stress, fiber area and depth at the middle of the fiber, respectively. F_R is the residual force, unbalanced force, at the end of each iteration and M is the calculated moment for each given curvature (χ) .

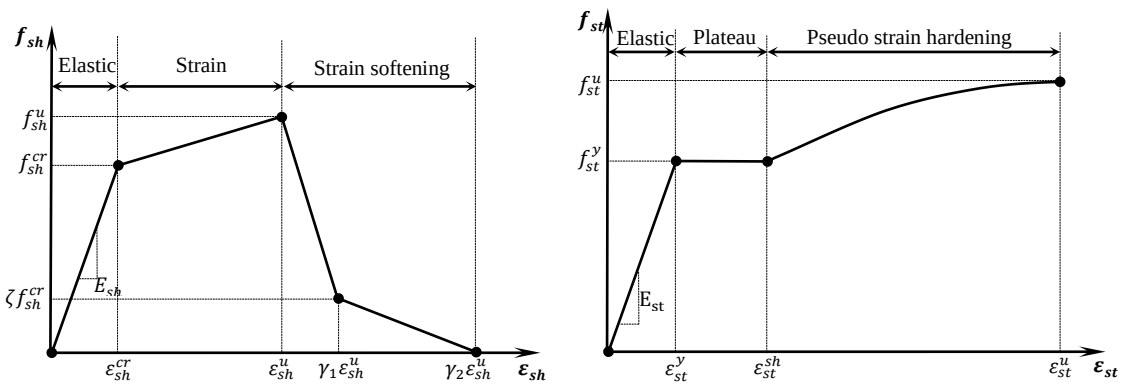

(a) (b)

Figure 13- Constitutive law to simulate tensile behaviour of (a) SHCC, and (b) steel reinforcement [27].

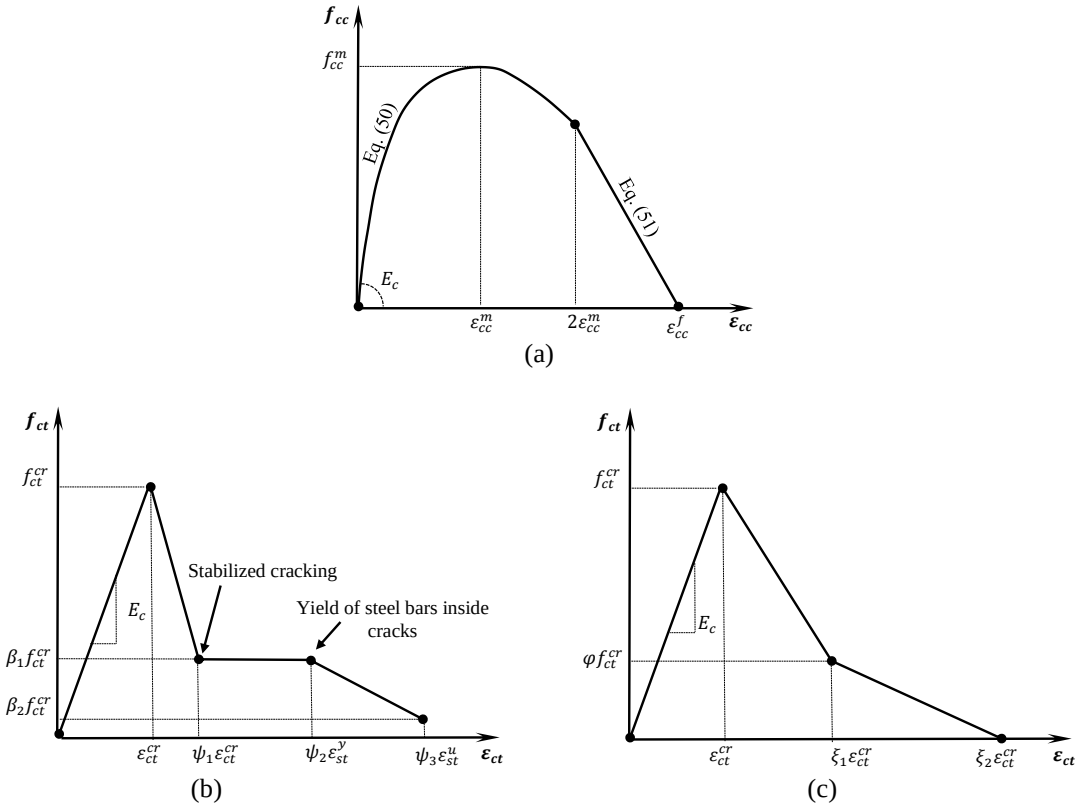

Figure 14- Adopted constitutive laws for concrete under (a) uniaxial compression [28], and under uniaxial tension, (b) for steel/FRP reinforced concrete (tension-stiffening in post-cracking), and (c) for plain concrete (tension-softening in post-cracking [30]) .

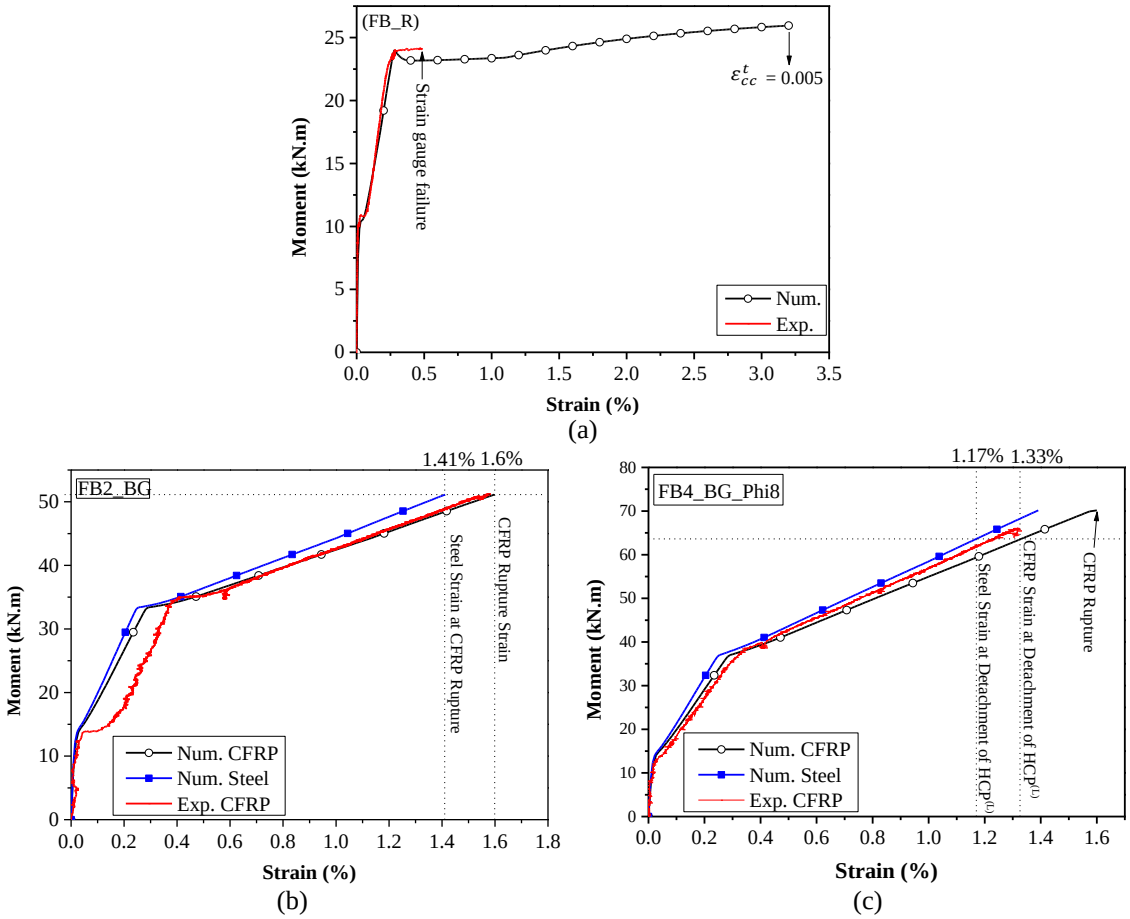

Figure 15- Comparison of the evolution of the mid-span strain in steel/CFRP reinforcement *versus* moment obtained from numerical and experimental studies in beam, (a) FB_R, (b) FB2_BG, and (c) FB4_BG_Phi8.

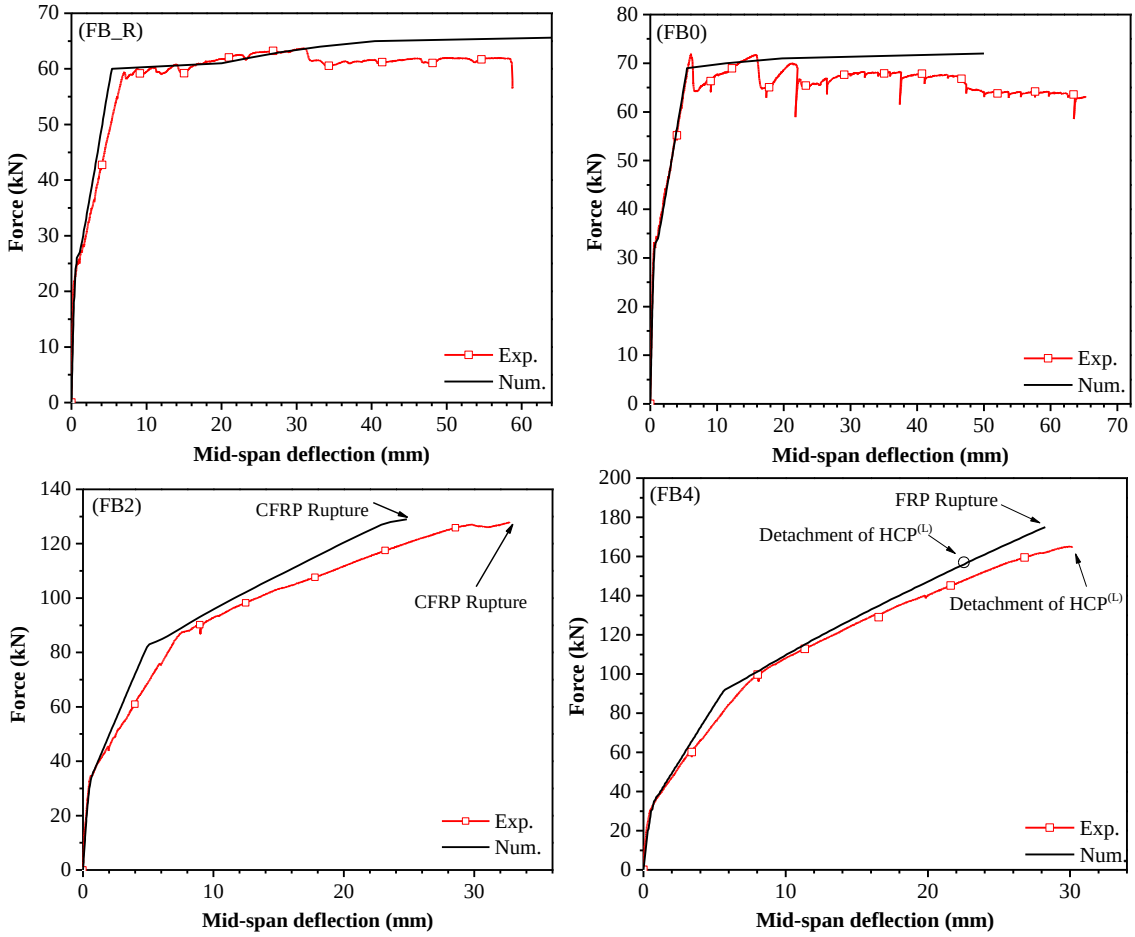

Figure 16- Comparison of the force-deflection curves obtained from numerical simulations with those of experimental tests.